

**C/2014 UN₂₇₁ (Bernardinelli-Bernstein): The Nearly Spherical Cow of Comets**

Pedro H. Bernardinelli¹ , Gary M. Bernstein¹ , Benjamin T. Montet^{2,3} , Robert Weryk⁴ , Richard Wainscoat⁵ , M. Agüena⁶ , S. Allam⁷, F. Andrade-Oliveira^{6,8}, J. Annis⁷ , S. Avila⁹, E. Bertin^{10,11} , D. Brooks¹² , D. L. Burke^{13,14}, A. Carnero Rosell⁶, M. Carrasco Kind^{15,16}, J. Carretero¹⁷ , R. Cawthon¹⁸ , C. Conselice^{19,20} , M. Costanzi^{21,22,23} , L. N. da Costa^{6,24}, M. E. S. Pereira^{25,26}, J. De Vicente²⁷, H. T. Diehl⁷ , S. Everett²⁸, I. Ferrero²⁹, B. Flaugher⁷, J. Frieman^{7,30}, J. García-Bellido⁹ , E. Gaztanaga^{31,32} , D. W. Gerdes^{25,33} , D. Gruen³⁴, R. A. Gruendl^{15,16} , J. Gschwend^{6,24} , G. Gutierrez⁷, S. R. Hinton³⁵ , D. L. Hollowood²⁸ , K. Honscheid^{36,37}, D. J. James³⁸, K. Kuehn^{39,40} , N. Kuropatkin⁷, O. Lahav¹², M. A. G. Maia^{6,24}, J. L. Marshall⁴¹ , F. Menanteau^{15,16} , R. Miquel^{17,42} , R. Morgan¹⁸ , R. L. C. Ogando²⁴, F. Paz-Chinchón^{15,43} , A. Pieres^{6,24} , A. A. Plazas Malagón⁴⁴, M. Rodríguez-Monroy²⁷, A. K. Romer⁴⁵, A. Roodman^{13,14} , E. Sanchez²⁷, M. Schubnell²⁵, S. Serrano^{31,32}, I. Sevilla-Noarbe²⁷ , M. Smith⁴⁶, M. Soares-Santos²⁵, E. Suchyta⁴⁷, M. E. C. Swanson¹⁵ , G. Tarle²⁵ , C. To^{13,14,48} , M. A. Troxel⁴⁹, T. N. Varga^{50,51}, A. R. Walker⁵², and Y. Zhang⁷

(The DES Collaboration)

¹ Department of Physics and Astronomy, University of Pennsylvania, Philadelphia, PA 19104, USA; pedrobe@sas.upenn.edu² School of Physics, University of New South Wales, Sydney, NSW 2052, Australia; garyb@physics.upenn.edu³ UNSW Data Science Hub, University of New South Wales, Sydney, NSW 2052, Australia⁴ Department of Physics & Astronomy, University of Western Ontario, 1151 Richmond Street, London, ON N6A 3K7, Canada⁵ Institute for Astronomy, University of Hawaii, 2680 Woodlawn Drive, Honolulu, HI 96822, USA⁶ Laboratório Interinstitucional de e-Astronomia—LIeA, Rua Gal. José Cristino 77, Rio de Janeiro, RJ—20921-400, Brazil⁷ Fermi National Accelerator Laboratory, P.O. Box 500, Batavia, IL 60510, USA⁸ Instituto de Física Teórica, Universidade Estadual Paulista, São Paulo, Brazil⁹ Instituto de Física Teórica UAM/CSIC, Universidad Autónoma de Madrid, E-28049 Madrid, Spain¹⁰ CNRS, UMR 7095, Institut d'Astrophysique de Paris, F-75014, Paris, France¹¹ Sorbonne Universités, UPMC Univ Paris 06, UMR 7095, Institut d'Astrophysique de Paris, F-75014, Paris, France¹² Department of Physics & Astronomy, University College London, Gower Street, London, WC1E 6BT, UK¹³ Kavli Institute for Particle Astrophysics & Cosmology, P.O. Box 2450, Stanford University, Stanford, CA 94305, USA¹⁴ SLAC National Accelerator Laboratory, Menlo Park, CA 94025, USA¹⁵ Center for Astrophysical Surveys, National Center for Supercomputing Applications, 1205 West Clark Street, Urbana, IL 61801, USA¹⁶ Department of Astronomy, University of Illinois at Urbana-Champaign, 1002 West Green Street, Urbana, IL 61801, USA¹⁷ Institut de Física d'Altes Energies (IFAE), The Barcelona Institute of Science and Technology, Campus UAB, E-08193 Bellaterra (Barcelona), Spain¹⁸ Physics Department, 2320 Chamberlin Hall, University of Wisconsin—Madison, 1150 University Avenue, Madison, WI 53706-1390, USA¹⁹ Jodrell Bank Center for Astrophysics, School of Physics and Astronomy, University of Manchester, Oxford Road, Manchester, M13 9PL, UK²⁰ University of Nottingham, School of Physics and Astronomy, Nottingham NG7 2RD, UK²¹ Astronomy Unit, Department of Physics, University of Trieste, via Tiepolo 11, I-34131 Trieste, Italy²² INFN—Osservatorio Astronomico di Trieste, via G.B. Tiepolo 11, I-34143 Trieste, Italy²³ Institute for Fundamental Physics of the Universe, Via Beirut 2, I-34014 Trieste, Italy²⁴ Observatório Nacional, Rua Gal. José Cristino 77, Rio de Janeiro, RJ—20921-400, Brazil²⁵ Department of Physics, University of Michigan, Ann Arbor, MI 48109, USA²⁶ Hamburger Sternwarte, Universität Hamburg, Gojenbergsweg 112, D-21029 Hamburg, Germany²⁷ Centro de Investigaciones Energéticas, Medioambientales y Tecnológicas (CIEMAT), Madrid, Spain²⁸ Santa Cruz Institute for Particle Physics, Santa Cruz, CA 95064, USA²⁹ Institute of Theoretical Astrophysics, University of Oslo, P.O. Box 1029 Blindern, NO-0315 Oslo, Norway³⁰ Kavli Institute for Cosmological Physics, University of Chicago, Chicago, IL 60637, USA³¹ Institut d'Estudis Espacials de Catalunya (IEEC), E-08034 Barcelona, Spain³² Institute of Space Sciences (ICE, CSIC), Campus UAB, Carrer de Can Magrans, s/n, 08193 Barcelona, Spain³³ Department of Astronomy, University of Michigan, Ann Arbor, MI 48109, USA³⁴ Faculty of Physics, Ludwig-Maximilians-Universität, Scheinerstr. 1, D-81679 Munich, Germany³⁵ School of Mathematics and Physics, University of Queensland, Brisbane, QLD 4072, Australia³⁶ Center for Cosmology and Astro-Particle Physics, The Ohio State University, Columbus, OH 43210, USA³⁷ Department of Physics, The Ohio State University, Columbus, OH 43210, USA³⁸ Center for Astrophysics | Harvard & Smithsonian, 60 Garden Street, Cambridge, MA 02138, USA³⁹ Australian Astronomical Optics, Macquarie University, North Ryde, NSW 2113, Australia⁴⁰ Lowell Observatory, 1400 Mars Hill Road, Flagstaff, AZ 86001, USA⁴¹ George P. and Cynthia Woods Mitchell Institute for Fundamental Physics and Astronomy, and Department of Physics and Astronomy, Texas A&M University, College Station, TX 77843, USA⁴² Institució Catalana de Recerca i Estudis Avançats, E-08010 Barcelona, Spain⁴³ Institute of Astronomy, University of Cambridge, Madingley Road, Cambridge CB3 0HA, UK⁴⁴ Department of Astrophysical Sciences, Princeton University, Peyton Hall, Princeton, NJ 08544, USA⁴⁵ Department of Physics and Astronomy, Pevensey Building, University of Sussex, Brighton, BN1 9QH, UK⁴⁶ School of Physics and Astronomy, University of Southampton, Southampton, SO17 1BJ, UK⁴⁷ Computer Science and Mathematics Division, Oak Ridge National Laboratory, Oak Ridge, TN 37831, USA⁴⁸ Department of Physics, Stanford University, 382 Via Pueblo Mall, Stanford, CA 94305, USA⁴⁹ Department of Physics, Duke University, Durham, NC 27708, USA⁵⁰ Max Planck Institute for Extraterrestrial Physics, Giessenbachstrasse, D-85748 Garching, Germany

⁵¹ Universitäts-Sternwarte, Fakultät für Physik, Ludwig-Maximilians Universität München, Scheinerstr. 1, D-81679 München, Germany

⁵² Cerro Tololo Inter-American Observatory, NSF's National Optical-Infrared Astronomy Research Laboratory, Casilla 603, La Serena, Chile
Received 2021 September 20; revised 2021 October 22; accepted 2021 October 22; published 2021 November 9

Abstract

Comet C/2014 UN₂₇₁ (Bernardinelli-Bernstein), incoming from the Oort cloud, is remarkable in having the brightest (and presumably largest) nucleus of any well-measured comet and having been discovered at the heliocentric distance $r_h \approx 29$ au, farther than any Oort cloud comet. In this work, we describe the discovery process and observations and the properties that can be inferred from images recorded until the first reports of activity in 2021 June. The orbit has $i = 95^\circ$, with a perihelion of 10.97 au to be reached in 2031 and a previous aphelion at $40,400 \pm 260$ au. Backward integration of the orbit under a standard Galactic tidal model and known stellar encounters suggests a perihelion of $q \approx 18$ au on its previous perihelion passage 3.5 Myr ago; hence, the current data could be the first ever obtained of a comet that has not been inside Uranus's orbit in 4 Gyr. The photometric data show an unresolved nucleus with absolute magnitude $H_r = 8.0$, colors that are typical of comet nuclei or Damocloids, and no secular trend as it traversed the range 34–23 au. For the r -band geometric albedo p_r , this implies a diameter of $150(p_r/0.04)^{-0.5}$ km. There is strong evidence of brightness fluctuations at the ± 0.2 mag level, but no rotation period can be discerned. A coma, nominally consistent with a “stationary” $1/\rho$ surface brightness distribution, grew in scattering cross section at an exponential rate from $Af\rho \approx 1$ to ≈ 150 m as the comet approached from 28 to 20 au. The activity rate is consistent with a very simple model of sublimation of a surface species in radiative equilibrium with the Sun. The inferred enthalpy of sublimation matches those of CO₂ and NH₃. More volatile species, such as N₂, CH₄, and CO, must be far less abundant on the sublimating surfaces.

Unified Astronomy Thesaurus concepts: [Long period comets \(933\)](#); [Small Solar System bodies \(1469\)](#); [Comet nuclei \(2160\)](#); [Comet dynamics \(2213\)](#); [Comet origins \(2203\)](#)

1. Introduction

Our knowledge of the content of the Oort cloud is highly fragmentary; all inferences are based upon the small subset of its members that are torqued into orbits with perihelia $q \lesssim 10$ au and, until recently, only the subset of these that develop comae bright enough to be noticed as comets. The cometary activity makes the objects easier to find and makes it easier to identify the composition of the surface volatiles, but it can also obscure the properties of the nuclear body. The diversity of Oort cloud bodies has only recently begun to be explored, with the discovery of objects having varying levels of activity beyond the water frost line at ≈ 5 au (Meech et al. 2009; Sárneczky et al. 2016; Jewitt et al. 2017, 2021; Meech et al. 2017; Hui et al. 2018, 2019). The discovery of C/2014 UN₂₇₁ (Bernardinelli-Bernstein) (hereafter BB) has expanded this known diversity substantially; as we will elaborate below, it is probably the largest Oort cloud comet ever found and likely similar in size to the largest body ever seen to exhibit cometary behavior, the Centaur (2060) Chiron (Bus et al. 1996; Sickafoose et al. 2020). Furthermore, the first high-quality observations were taken when BB was at heliocentric distance $r_h \approx 29$ au in 2014, well before the first announced detection of a coma in 2021 June at $r_h \approx 20$ au. In this work, we will summarize the observations in which BB was discovered and the inferences about its composition and history that can be made from these and other images taken until the recent first announcement of detectable activity.

Comet BB was discovered as part of the search for trans-Neptunian objects (TNOs) in the 80,000 exposures taken by the Dark Energy Survey (DES) in the period 2013–2019 described fully in Bernardinelli et al. (2021). We refer to this paper for details of how ≈ 108 million single-night transient detections were identified and potential TNOs linked from among them. The

discovery of BB was somewhat fortuitous because the search algorithms targeted objects at $r_h \geq 29$ au, while BB was closer than this for all but its first DES exposures. The DES search should therefore not be used to estimate the density of Oort cloud comets like BB, though we can say that any object having $r_h > 29$ au and $m_r < 23.8$ for >2 yr of DES observing and lying within the 5000 deg² footprint of DES (see Figure 5 of Bernardinelli et al. 2021) would have a high probability of detection.

Comet BB appears in 42 DES survey images in the grizY filters on 25 distinct nights spanning 10 Oct 2014 to 26 Nov 2018. Some of these images have artifacts that preclude precision photometry and/or astrometry, leaving 32 useful astrometric measures on 21 distinct nights and 40 useful flux measures. The Solar System Object Image Search service (Gwyn et al. 2012) finds additional archival imaging of BB from the Wide-field Infrared Survey Explorer (WISE), CFHT, VST, VISTA, and Pan-STARRS observatories. One VISTA z -band coadded series of dithered exposures from 2010 October 20 contains a measurable image of BB, extending the arc and photometric record to $r_h = 34.1$ au. We measure the positions and gri fluxes of BB in a series of four CFHT exposures taken just before the first DES exposures but do not attempt to measure the contemporaneous u -band exposure, which has only a marginal detection. The object is not detectable in WISE images taken during its primary mission in 2010 (E. Wright, private communication). We did not attempt to recover BB from the VST images, even though some are previous to the DES epoch, since these have shorter exposures on a smaller telescope. We also extract magnitudes from the TESS spacecraft imaging of the comet as it traversed Sector 3 in 2018 September–October and Sectors 29/30 in 2020 August–October. Circumstances, positions, fluxes, and uncertainties for BB in these exposures are listed in Table 2, with the TESS series each combined into a single mean flux.

Within 24 hr of publication of the DES discovery in MPEC 2021-M53 (Bernardinelli & Bernstein 2021) on 2021 June 19, images were taken showing a visible coma (Buzzi & Lister 2021;



Original content from this work may be used under the terms of the [Creative Commons Attribution 4.0 licence](#). Any further distribution of this work must maintain attribution to the author(s) and the title of the work, journal citation and DOI.

Table 1
Osculating Barycentric Orbital Elements

Epoch	a (au)	e	i	Ω	ω	t_{peri} (JD)
1950	20, 200 \pm 130	0.999458(4)	95°4663	190°0029	326°2793(3)	2,462,887.94(4)
2100	28, 070 \pm 170	0.999610(2)	95°4606	190°0093	326°2438(4)	2,462,887.87(9)

Note. Elements are given at epochs before and after the current passage through the realm of the giant planets, assuming only gravitational forces. Uncertainties in the last digit are given in parentheses where they are sufficiently large.

Demetz et al. 2021; Kokotanekova et al. 2021a). Analysis of the TESS data of BB indicated a large coma in 2018 (Farnham 2021) and no detectable rotation period (Ridden-Harper et al. 2021).

This paper will analyze the behavior of the comet as evidenced from these observations through 2021 June. In the next section, we examine the recent dynamics of BB. Section 3 examines the properties of the comet nucleus, and Section 4 examines the onset of activity over the period 2010–2021.

2. Astrometric Properties

2.1. Measurements

The DES astrometry is mapped to Gaia DR2 (Gaia Collaboration et al. 2018) using the astrometric model presented in Bernstein et al. (2017).⁵³ All distortions due to the telescope, instrument, and detectors are known to ≈ 1 mas rms, and the color-dependent effects (differential chromatic refraction in the atmosphere and lateral color distortions) are corrected using the object’s mean $g - i$ color. The position uncertainties for the DES exposures (2014–2018) include the shot noise from each detection, as well as an anisotropic contribution from the atmospheric turbulence (Bernardinelli et al. 2020). For the VISTA (2010) and CFHT (2014) images, we retrieve detrended images from the archives, remeasure the positions using SExtractor windowed centroiding, and produce a polynomial astrometric solution in the vicinity of BB by referencing nearby stars from the Gaia DR2 catalog. Astrometry for the PanSTARRS1 (PS1; 2014–2019) exposures is extracted using Gaussian fits to the comet and field stars, with the latter referenced to DR2. One PS1 exposure with a barely detectable signal-to-noise ratio (S/N) is a $>3\sigma$ outlier from the orbit fit and excluded from further consideration.

2.2. Orbital Properties and Previous Perihelion

We determine the object’s orbit using the method of Bernstein & Khushalani (2000), and we do not include nongravitational forces in the orbit fit, as these have not been detected for BB yet. The orbital elements and derived uncertainties are presented in Table 1 and yield $\chi^2/\text{dof} = 116.5/96$. Considering only DES observations yields a consistent orbit with $\approx 1.5\times$ larger uncertainties and $\chi^2/\text{dof} = 66.4/58$. The semimajor axis and inclination of the incoming orbit are 20,200 au and 95°5, respectively, fully characteristic of Oort cloud membership. Perihelion of 10.95 au will be reached on 2031 January 21. Forward integration of the orbit for ≈ 50 yr shows that the semimajor axis will be increased by 40% after this perihelion.

It is of substantial interest to determine whether BB has been appreciably warmed on previous perihelion passages. We study the past dynamics of BB using a numerical procedure similar to that of Królikowska & Dybczyński (2018), and also by analytic

approximations. We will consider perturbations by the Galactic tidal tensor \mathcal{G} , assumed (as in Heisler & Tremaine 1986) to be diagonal in the Galactic frame rotating with the Sun, where \hat{x} points to the Galactic center and \hat{z} points to the north Galactic pole. This translates to a contribution to the Hamiltonian of the system in the form (Fouchard 2004)

$$\mathcal{H}_G = \frac{1}{2} \mathbf{x} \cdot \mathcal{G} \cdot \mathbf{x} = \mathcal{G}_1 \frac{x^2}{2} + \mathcal{G}_2 \frac{y^2}{2} + \mathcal{G}_3 \frac{z^2}{2}. \quad (1)$$

We adopt the nominal Oort constants (Oort 1927) $A = 15.1$ and $B = -13.4 \text{ km s}^{-1} \text{ kpc}^{-1}$ from Li et al. (2019) and a local stellar density $\rho_0 = 0.15 M_\odot \text{ pc}^{-3}$ from Vokrouhlický et al. (2019), so we have $\mathcal{G}_1 \equiv -(A - B)(3A + B) = -9.49 \times 10^{-16}$, $\mathcal{G}_2 \equiv (A - B)^2 = 8.48 \times 10^{-16}$, and $\mathcal{G}_3 \equiv 4\pi\mu\rho_0 - 2(B^2 - A^2) = 8.59 \times 10^{-15} \text{ yr}^{-2}$. The angular velocity of the Sun is $\Omega_0 \equiv B - A = -28.5 \text{ km s}^{-1} \text{ kpc}^{-1} = -2.91 \times 10^{-8} \text{ yr}^{-1}$.

The numerical approach is to integrate, backward in time, clones of the orbit solution sampled from the state vector covariance matrix. We use the WHFAST (Wisdom & Holman 1991; Rein & Tamayo 2015) integrator of REBOUND (Rein & Liu 2012) and include the giant planets as active perturbers, as well as the effects of the Galactic tide using REBOUNDX (Tamayo et al. 2020). Figure 1 shows the histogram of the previous orbit perihelion distance and time from numerical integration of the sampled orbits, which are near 18.2 au and 3.41 Myr, respectively.

Analytically, we calculate the change in angular momentum ΔL imparted by the tidal torque over a full orbit in the limit where the orbit is fully radial, $e \rightarrow 1$. Near this limit, $L^2 = 2kq$, where k is the barycentric gravitational constant $1.0014 GM_\odot$, and q is the perihelion. We define \hat{e} as the unit vector toward perihelion (inverse of aphelion direction). The Born approximation then yields $\Delta L = 5\pi \sqrt{\frac{a^7}{k}} \hat{e} \times (\mathcal{G} \cdot \hat{e})$. This yields a previous perihelion of 18.3 au for the nominal orbit, in agreement with the numerical integration.

The ascending node of the previous passage has $r_h \approx 20$ au in the numerical integrations, suggesting the possibility that an encounter with Uranus had significantly altered the orbit, and some earlier perihelion had been < 18 au. The chances of a sufficiently close Uranus encounter are very low, however. If BB encountered Uranus at impact parameter b with relative speed v at heliocentric distance r_h , then the impulse was $I = 2GM_U/bv$, and the maximum change in specific angular moment would be $|\Delta L| \leq I r_h$. Since BB is in a near-parabolic orbit that is nearly perpendicular to the ecliptic, we have

$$\frac{|\Delta L|}{|L|} \leq \frac{I r_h}{\sqrt{2GM_\odot q}} \quad (2)$$

$$\leq \frac{2GM_U r_h}{b} \sqrt{\frac{r_h}{2GM_\odot}} \frac{1}{\sqrt{2GM_\odot q}} \quad (3)$$

⁵³ Astrometric solutions were derived before the release of Gaia EDR3.

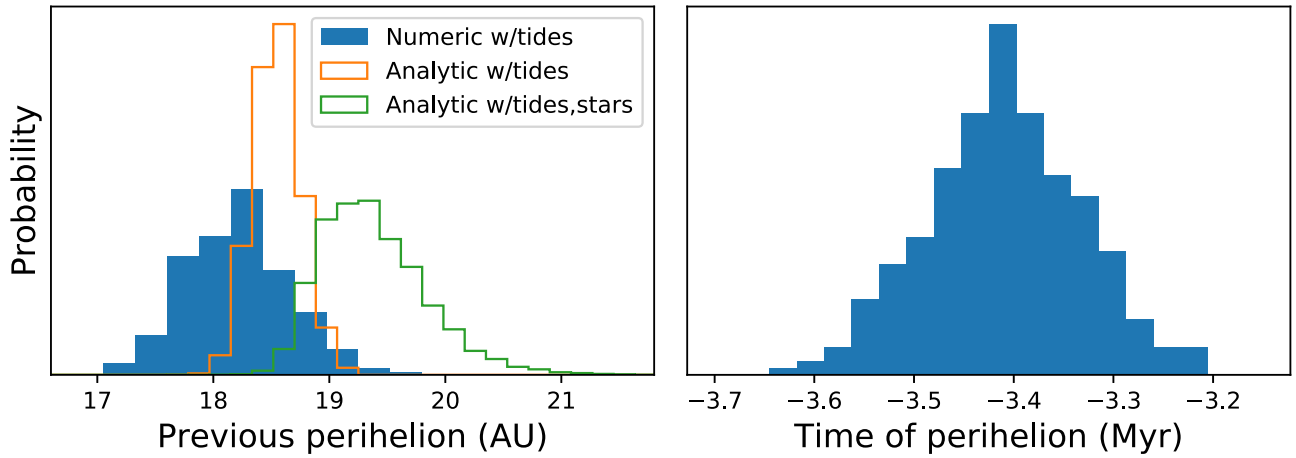


Figure 1. Distribution of properties of the previous perihelion of BB. The filled histograms show the predicted perihelion and its time of occurrence in backward numerical integrations incorporating the giant planets and Galactic tides. The orange and green open histograms show the result of analytic approximations that treat the solar system as a point mass and use the Born approximation to a plunging comet orbit. Both incorporate Galactic tides; the green histogram also includes the impulse approximation to the influence of eight closely approaching stars identified from the Gaia catalogs. All plots marginalize over the uncertainties in the dynamical state of BB and the stellar encounters. In all cases, the previous perihelion is higher, 17–21 au, than the current $q = 11$ au and occurred ≈ 3.4 Myr ago.

$$= \frac{M_U r_h}{M_\odot b} \sqrt{\frac{r_h}{q}} \quad (4)$$

$$\approx 5 \times 10^{-5} \frac{20 \text{ au}}{b}. \quad (5)$$

For this perturbation of the angular momentum (and perihelion) to be as large as 10% requires $b < 0.01$ au. The chances that Uranus is this close to BB’s previous node are $< 0.01\%$ given the 120 au circumference of Uranus’s orbit.

We may also use the impulse approximation to assess the angular momentum imparted by passages of stars close to the Sun during the previous orbit. For a star with mass M_* with a closest approach to the Sun at point \mathbf{b} and velocity \mathbf{v} , while the comet is at position \mathbf{r} , the angular momentum imparted is

$$\Delta L = \frac{2GM_*}{v} \mathbf{r} \times \left[\mathbf{b} \left(\frac{1}{|\mathbf{b}'|^2} - \frac{1}{|\mathbf{b}|^2} \right) + \hat{\mathbf{v}} \frac{\mathbf{r} \cdot \hat{\mathbf{v}}}{|\mathbf{b}'|^2} \right], \quad (6)$$

$$\mathbf{b}' = \mathbf{b} - \mathbf{r} + \hat{\mathbf{v}}(\mathbf{r} \cdot \hat{\mathbf{v}}). \quad (7)$$

We use the list of reliable close stellar encounters ($b < 1$ pc) derived from the Gaia DR2 catalog by Bailer-Jones et al. (2018), restricted to those with perihelion times $-4 \text{ Myr} < t_{\text{ph}} < 0 \text{ Myr}$ relative to present. We updated the stellar parameters for each star to the values and uncertainties given in Gaia EDR3 (Gaia Collaboration et al. 2021). This removes a very strong perturber from this list (DR2 955098506408767360) and some others, leaving eight potential encounters over BB’s previous orbit (see also Bobylev & Bajkova 2020). We assume linear motion for the perturbing stars and sample from the Gaia uncertainties. The net effect of these encounters is to slightly decrease L , i.e., to raise the previous perihelion by an amount that is well below the effect of the Galactic tide. The left panel of Figure 1 shows the histograms of previous perihelion distances derived from the analytic approximations for the Galactic tide alone (orange; sampling from BB’s orbital uncertainties) and for the Galactic tide plus stellar encounters (green).

The conclusion, which is robust to the details of the tidal model or these eight stars’ dynamics, is that the previous

passage of BB was further from the Sun than the current one. Indeed, under the tidal model, the perihelion has been getting smaller with each successive passage for many orbits into the past. We conclude that BB is a “new” comet in the sense that there is no evidence for a previous approach closer than 18 au to the Sun since ejection into the Oort cloud. Indeed, the observations of BB may be the first ever obtained for an object that has not crossed within Uranus’s orbit since the solar system formation epoch. It remains true, however, that our knowledge of stellar encounters is incomplete, and it is possible that some yet-unknown star’s passage could have lifted BB’s perihelion from a lower value to its present one.

3. Nuclear Properties

The images of BB in 2018 and earlier exhibit a central unresolved source plus a very low surface brightness coma or tail. In this section, we will fit point-source magnitudes to the comet. The measures of diffuse flux in Section 4 confirm that potential contamination of these point-source fluxes by coma flux will be small for the DES data. Therefore, we will treat them as nuclear magnitudes, with the caveat that small outbursts could perturb the point-source measures for some period of time before they disperse out of the central arcsecond. Note that $1''$ subtends 2×10^7 m at 25 au; dust grains traveling at 10 m s^{-1} will travel this distance in < 1 month. Higher diffuse surface brightness is present in the images after 2018, and we will not use these in attempts to characterize the nucleus but will return to them when characterizing the coma.

3.1. Measurements

We measure the flux in each DES image using scene-modeling photometry, similar to Brout et al. (2019). We define a target region around each detection of 272×272 pixels (at $0''.264 \text{ pixel}^{-1}$) and simultaneously fit a model for the object’s flux and the background sources to all DES images from the same filter in this region of the sky. The background is modeled as a grid of point sources that is present in all images, while the object is modeled as a point source present in only the detection image. Each point source is convolved with the point-spread

Table 2
Observational Data for C/2014 UN₂₇₁

UTC	R.A.	Decl.	Error	Source	Mag	Band	Helio. Dist. (au)	Geo. dist. (au)
2010-11-15.238223	01:19:36.7532	-30:42:27.260	0 ^s .105	VISTA	22.47 ± 0.26	<i>z</i>	34.07	33.52
2014-08-14.599780	01:42:23.9960	-35:36:37.600	0 ^s .078	PS1	23.10 ± 0.20*	<i>i</i>	29.28	28.74
2014-08-28.601410	01:41:25.1473	-36:02:11.803	0 ^s .04	CFHT	22.39 ± 0.09	<i>r</i>	29.23	28.59
2014-08-28.606693	01:41:25.1180	-36:02:12.397	0 ^s .09	CFHT	23.05 ± 0.08	<i>g</i>	29.23	28.59
2014-08-28.609338	01:41:25.1015	-36:02:12.632	0 ^s .06	CFHT	22.14 ± 0.17	<i>i</i>	29.23	28.59
2014-08-28.612016	01:41:25.0891	-36:02:13.023	0 ^s .04	CFHT	22.69 ± 0.12	<i>r</i>	29.23	28.59
2014-10-20.294348	01:34:35.0187	-37:14:46.144	0 ^s .068	DES	22.62 ± 0.10	<i>r</i>	29.05	28.36
2014-11-04.122035	01:32:21.0290	-37:23:21.138	0 ^s .050	DES	22.09 ± 0.12	<i>z</i>	28.99	28.41
2014-11-14.258286	DES	21.93 ± 0.46	<i>Y</i>	28.96	28.46
2014-11-15.251906	01:30:47.0392	-37:25:39.196	0 ^s .047	DES	22.32 ± 0.16	<i>z</i>	28.95	28.47
2014-11-18.235595	01:30:23.4255	-37:25:40.010	0 ^s .040	DES	22.52 ± 0.05	<i>r</i>	28.94	28.49
2014-11-18.238347	01:30:23.4067	-37:25:39.984	0 ^s .041	DES	22.22 ± 0.07	<i>i</i>	28.94	28.49
2014-11-27.221480	01:29:17.5832	-37:24:12.514	0 ^s .113	DES	...	<i>g</i>	28.91	28.55
2014-12-11.115676	01:27:54.8295	-37:17:49.638	0 ^s .084	DES	22.43 ± 0.09	<i>i</i>	28.86	28.67
2014-12-11.144452	DES	22.57 ± 0.62	<i>Y</i>	28.86	28.67
2015-01-09.107010	01:26:35.3245	-36:51:38.750	0 ^s .130	DES	22.65 ± 0.30	<i>z</i>	28.76	28.94
2015-08-11.612980	01:47:05.4300	-37:26:12.860	0 ^s .102	PS1	23.33 ± 0.22*	<i>i</i>	27.99	27.49
2015-08-17.357470	01:46:47.5049	-37:37:39.814	0 ^s .053	DES	22.64 ± 0.08	<i>r</i>	27.97	27.42
2015-08-17.358826	01:46:47.5170	-37:37:39.886	0 ^s .080	DES	22.99 ± 0.09	<i>g</i>	27.97	27.42
2015-08-24.344520	01:46:18.6053	-37:51:28.614	0 ^s .060	DES	23.12 ± 0.09	<i>g</i>	27.94	27.35
2015-08-24.347311	DES	22.53 ± 0.07	<i>r</i>	27.94	27.35
2015-08-24.348700	DES	22.38 ± 0.08	<i>i</i>	27.94	27.35
2015-09-01.306625	DES	22.46 ± 0.54	<i>Y</i>	27.92	27.27
2015-09-02.377866	01:45:30.1964	-38:08:52.304	0 ^s .085	DES	21.94 ± 0.28	<i>Y</i>	27.91	27.26
2015-09-13.390509	01:44:15.8625	-38:28:51.622	0 ^s .073	DES	22.47 ± 0.10	<i>i</i>	27.87	27.17
2015-10-06.274354	01:40:59.7742	-39:03:19.836	0 ^s .147	DES	22.18 ± 0.17	<i>z</i>	27.79	27.08
2015-11-20.228513	01:33:55.0781	-39:29:32.567	0 ^s .067	DES	22.18 ± 0.14	<i>z</i>	27.63	27.21
2015-11-20.235561	01:33:55.0098	-39:29:32.478	0 ^s .058	DES	22.50 ± 0.11	<i>i</i>	27.63	27.21
2016-01-11.093863	01:29:57.7382	-38:50:26.056	0 ^s .044	DES	22.45 ± 0.06	<i>r</i>	27.44	27.64
2016-01-11.095236	01:29:57.7285	-38:50:25.964	0 ^s .055	DES	23.08 ± 0.09	<i>g</i>	27.44	27.64
2016-08-09.585360	01:52:24.3560	-39:29:37.720	0 ^s .090	PS1	23.53 ± 0.18*	<i>w</i>	26.68	26.21
2016-08-09.595282	01:52:24.3230	-39:29:39.130	0 ^s .129	PS1	23.45 ± 0.22*	<i>w</i>	26.68	26.21
2016-10-01.297615	DES	22.10 ± 0.07	<i>i</i>	26.49	25.80
2016-10-01.298994	01:46:40.1803	-41:11:31.779	0 ^s .043	DES	22.16 ± 0.05	<i>r</i>	26.49	25.80
2016-10-01.300363	01:46:40.1727	-41:11:32.002	0 ^s .069	DES	22.63 ± 0.05	<i>g</i>	26.49	25.80
2016-10-03.314076	DES	22.43 ± 0.10	<i>i</i>	26.48	25.80
2016-10-03.315455	01:46:20.1770	-41:14:24.527	0 ^s .038	DES	22.36 ± 0.05	<i>r</i>	26.48	25.80
2016-10-03.316819	01:46:20.1667	-41:14:24.592	0 ^s .050	DES	22.81 ± 0.07	<i>g</i>	26.48	25.80
2017-08-13.571449	01:58:27.6990	-41:56:20.770	0 ^s .114	PS1	22.52 ± 0.18*	<i>i</i>	25.34	24.86
2017-08-14.585122	01:58:24.7020	-41:58:43.760	0 ^s .054	PS1	21.70 ± 0.09*	<i>i</i>	25.34	24.85
2017-09-08.554246	01:56:09.8760*	-42:55:16.230*	0 ^s .102	PS1	22.00 ± 0.20*	<i>i</i>	25.24	24.62
2017-09-30.421878	01:52:49.6350	-43:36:32.720	0 ^s .112	PS1	21.96 ± 0.15*	<i>i</i>	25.16	24.51
2017-10-15.272083	01:50:05.7460	-43:57:07.295	0 ^s .056	DES	22.29 ± 0.05	<i>g</i>	25.11	24.49
2017-10-15.337769	01:50:04.9880	-43:57:11.797	0 ^s .063	DES	21.42 ± 0.08	<i>z</i>	25.11	24.49
2017-10-15.339148	01:50:04.9697	-43:57:11.890	0 ^s .031	DES	21.69 ± 0.04	<i>r</i>	25.11	24.49
2017-10-29.358251	01:47:22.7320	-44:09:45.240	0 ^s .145	PS1	21.54 ± 0.20*	<i>i</i>	25.06	24.52
2017-11-06.330497	01:45:51.8610	-44:13:42.320	0 ^s .131	PS1	22.08 ± 0.21*	<i>i</i>	25.03	24.54
2017-12-11.250030	01:40:25.1950	-44:04:24.940	0 ^s .127	PS1	22.01 ± 0.15*	<i>w</i>	24.90	24.76
2017-12-15.180418	01:39:59.8371	-44:00:56.398	0 ^s .029	DES	22.05 ± 0.04	<i>r</i>	24.89	24.79
2017-12-15.181814	01:39:59.8244	-44:00:56.379	0 ^s .049	DES	22.58 ± 0.06	<i>g</i>	24.89	24.79
2017-12-25.149228	DES	21.87 ± 0.29	<i>Y</i>	24.85	24.87
2018-09-10.355826	DES	22.06 ± 0.03	<i>g</i>	23.90	23.31
2018-10-04	TESS	20.29 ± 0.15	<i>T</i>	23.82	23.21
2018-10-21.243368	01:55:54.0391	-46:47:14.935	0 ^s .075	DES	21.60 ± 0.17	<i>Y</i>	23.75	23.20
2018-10-27.178589	01:54:38.2037	-46:52:42.842	0 ^s .041	DES	21.59 ± 0.07	<i>z</i>	23.73	23.21
2018-11-08.235135	01:52:05.9144	-46:59:29.069	0 ^s .022	DES	21.71 ± 0.03	<i>r</i>	23.69	23.25
2018-11-08.236509	01:52:05.8988	-46:59:29.102	0 ^s .026	DES	21.51 ± 0.04	<i>i</i>	23.69	23.25
2018-11-08.237892	01:52:05.8841	-46:59:29.051	0 ^s .032	DES	22.23 ± 0.04	<i>g</i>	23.69	23.25
2019-08-19.598297	02:14:55.2390	-47:31:52.370	0 ^s .109	PS1	...	<i>i</i>	22.64	22.18
2019-08-29.569869	02:14:08.3560	-47:59:21.660	0 ^s .188	PS1	...	<i>w</i>	22.61	22.10
2019-08-29.585234	02:14:08.2450	-47:59:24.350	0 ^s .149	PS1	...	<i>w</i>	22.61	22.10
2019-08-29.592922	02:14:08.2250	-47:59:25.260	0 ^s .144	PS1	...	<i>w</i>	22.61	22.10
2020-09-21	TESS	18.24 ± 0.15	<i>T</i>	21.18	20.67

Note. Data marked with an asterisk are considered unreliable and not used in the analyses. Magnitudes for the 2019 PS1 observations are aperture-dependent, so they are not tabulated here.

function (PSF; see Jarvis et al. 2021 for a detailed description of the DES PSF model) of each pixel location in each exposure. This procedure also allows us to measure fluxes in exposures in

which there is no detection of the object but the orbit indicates its presence. Thus, as seen in Table 2, there are DES images having photometry but no useful astrometric data. The resultant

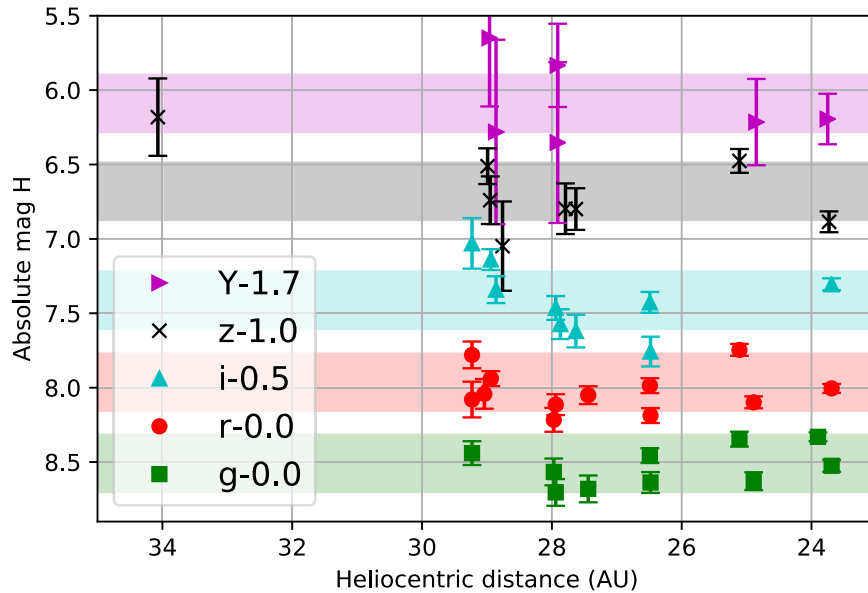


Figure 2. Photometry of BB plotted vs. heliocentric distance (bright is up, time runs to the right). This combines observations from DES, CFHT, and VISTA. For clarity, we have shifted the i , z , and Y data by the amounts noted in the legend. The horizontal colored bands are centered on the mean H_b determined for each band b and have the width of the best-estimate ± 0.20 mag of light-curve variation.

fluxes and errors are rigorously correct for an unresolved image, essentially using the central few arcseconds’ signal, and thus insensitive to any coma that does not have a central concentration. Flux calibration for all DES exposures is determined to mmag precision, as described in the Dark Energy Survey Collaboration (2021).

For the VISTA and CFHT detections, we acquire detrended images from their respective archives⁵⁴ and use `MAG_AUTO` measurements from `SExtractor` (Bertin & Arnouts 1996). Each exposure is placed on the DES magnitude system by choosing a zero-point to match the magnitudes found in the DES coadd catalogs in the corresponding filter for matching objects in the field. Bandpass differences between the VISTA z and CFHT gri filters and their DES counterparts lead to color corrections that are well below the measurement errors on these points and are ignored.

The PS1 photometry given in Table 2 is derived by fitting Gaussians to the comet images and stars of known magnitude (the w -band images use r -band magnitudes of the standards) and scaling the Gaussian fits. This photometry is less reliable and has a lower S/N than the DES data, so we will not make use of it in characterizing the nucleus. The PS1 measurements taken in 2019 are, however, valuable for characterizing the development of a coma between the end of DES in 2018 and the 2021 recoveries. We extract aperture photometry for these images around the predicted positions of BB to form the curves of growth shown in Section 4. The magnitude zero-points of the i and w images are determined by comparison of $6''$ diameter aperture photometry of bright stars to their i - and r -band magnitudes in the DES catalogs. The color terms between the PS1 and DES bands are again well below the measurement errors (Equation (B6) of the Dark Energy Survey Collaboration 2021).

TESS observations consist of “sectors,” $24^\circ \times 96^\circ$ regions of the sky observed nearly continuously for approximately 4 weeks (Ricker et al. 2015). In its survey of the southern sky,

TESS observed BB in three sectors, one in late 2018 and two in late 2020. For all three sectors, we identify and cut out an approximately $1.5^\circ \times 0.5^\circ$ region of the TESS full-frame images along the path of the comet with the `tesscut` tool (Brasseur et al. 2019). We then apply a difference imaging scheme aimed toward removing background stars by, for each frame and pixel, subtracting the mean flux observed in that pixel in all cadences observed between 5 and 10 hr from the time of the frame of interest.

At each frame, we then measure the flux of the target in an aperture of 5×5 of TESS’s $21''$ pixels. We apply the same method to nearby stars on the detector with low ($<1\%$) levels of photometric variability and well-characterized TESS magnitudes to transform our measured fluxes to magnitudes. The scatter of the residuals for stars on this scale is 0.15 mag, likely due to crowding of faint stars and intrapixel sensitivity variations on the TESS detector (Vorobiev et al. 2019). These issues should be less dramatic for BB due to its motion across the detector; nonetheless, we apply this 0.15 mag uncertainty conservatively on the individual magnitudes. The brightening of 2.01 ± 0.04 mag between the two TESS epochs is more reliably determined than the magnitude at either epoch. For an object of solar color, we should find $r - T = r_\odot - T_\odot = 4.61 - 4.26 = 0.35$ mag (Stassun et al. 2018; Willmer 2018).

3.2. Color, Variability, and Size

We fit all of the valid photometry from VISTA, CFHT, and DES to a model in which there is a fixed absolute magnitude H_b in each band b and an achromatic light-curve fluctuation $\Delta H = A \sin \phi$. These data are plotted in Figure 2. The illumination phase is between 1.4 and 2.5 for all observations here, so we ignore the phase terms in converting observed magnitudes to H . We have insufficient data to determine the light-curve phases ϕ_i for each exposure, so we consider each observation to have a random, independent $\phi_i \in [0, 2\pi]$. The posterior probability of the light-curve amplitude and the “true” H_b , given observations of H_i in band b_i with uncertainty σ_i for

⁵⁴ http://archive.eso.org/wdb/wdb/adp/phase3_vircam/form and <https://www.cadc-ccda.hia-ihc.nrc-cnrc.gc.ca/en/cfht/>.

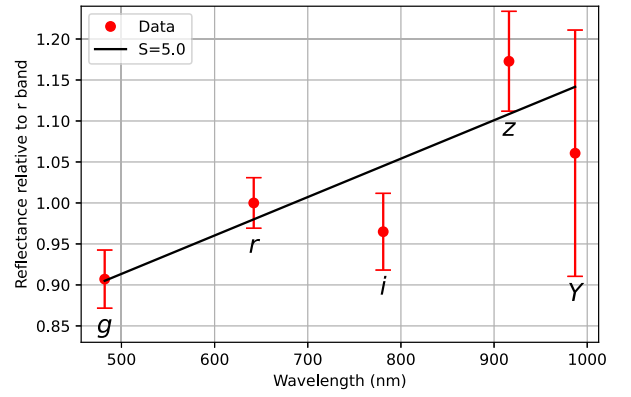
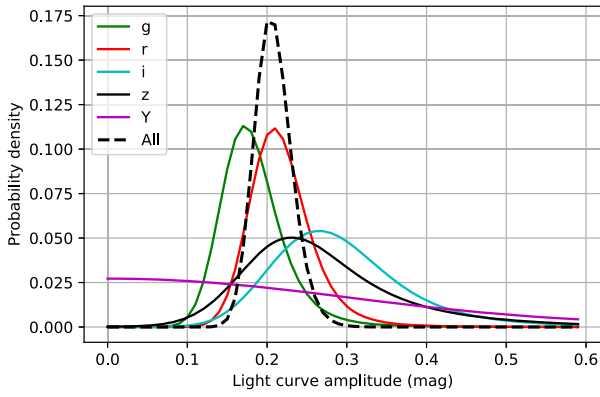


Figure 3. Left: posterior probability of the amplitude A of the comet light-curve variations $\Delta H = A \sin \phi$ as derived from 2018 and earlier. The individual bands’ constraints are consistent, and the combined result of $A = 0.20 \pm 0.03$ mag strongly excludes a constant absolute magnitude. Right: relative surface reflectance of BB, normalized to the nominal r -band value, plotted vs. wavelength. The symbols are derived from the mean H values found from maximizing the probability in Equation (8). The solid line is a model of the linear dependence of reflectance on wavelength, with the best-fit slope of $S = 5\%$ per 100 nm. This is similar to but slightly more neutral than the colors reported for other long-period comet (LPC) nuclei.

each observation i , is

$$p(A, \{H_b\} | \{H_i, \sigma_i\}) \propto \prod_{i \in \text{obs}} \int d\phi \exp[-(H_i - H_b - A \sin \phi)^2 / 2\sigma_i^2]. \quad (8)$$

Figure 3 (left) plots the posterior probability for the light-curve semiamplitude A . All of the bands are consistent and combine to yield $A = 0.20 \pm 0.03$ mag. This is a strong detection of variability in excess of the measurement errors. From Figure 2, it is clear that most of this variability is in short-term variation, not a long-term trend, consistent with a nuclear body with 10%–20% departures from sphericity. Ridden-Harper et al. (2021) reported a nondetection of variation in the TESS photometric time series, though no upper limit is reported. The TESS photometry has the majority of its flux coming from the coma, which will suppress the amplitude of any nuclear light curve, and hence does not exclude the possibility of ± 0.2 mag of nuclear variation.

Unresolved outbursts could also change the measured “point-source” fluxes. We can conclude, though, that the $\pm 20\%$ fluctuations are upper bounds for both fluctuations from outbursts and for nuclear variability. Thus, BB’s nucleus is close either to sphericity or to pole-on rotation.

The fitting process yields estimates of the mean absolute magnitude of the comet of $H = \{8.51 \pm 0.04, 7.96 \pm 0.03, 7.91 \pm 0.05, 7.68 \pm 0.06, 7.79 \pm 0.14\}$ in the $grizY$ bands, respectively. Figure 3 (right) plots the implied reflectivity in each band, normalized to unity in the r band, showing a color only slightly redder than neutral and perhaps even slightly blue in $r-i$. Jewitt (2015) presented colors for various outer solar system bodies quantified by a fit to a model of linear reflectance versus wavelength with a slope of $S\%$ per 100 nm when normalized to unit reflectivity at 550 nm (V band). Fitting the above H values (omitting Y) to such a model yields $S = 4.9 \pm 1.4$, with $\chi^2/\text{dof} = 4.4/2$. The solid line in the right panel of Figure 3 shows the $S = 5$ law.

An alternative method of deriving colors for BB is to find pairs of exposures taken in different bands within 5–10 minutes of each other, so that light-curve variations are unimportant. This results in color estimates of $g-r = 0.49 \pm 0.01$, $r-i = 0.22 \pm 0.02$, $i-z = 0.32 \pm 0.09$, and $g-z = 0.87 \pm 0.04$. These agree with the mean- H method, except that the pair-based $r-i$ color is

significantly redder. Fitting the 24 closely timed observations from 10 distinct nights to the linear-reflectance model yields $S = 6.1 \pm 1.1$, with $\chi^2/\text{dof} = 15.1/13$, in good agreement with the value derived from the H values.

Jewitt (2015) reported that potential relatives of BB, namely LPC nuclei and Damocloids, have typical S values of 10 and 15, respectively. These Oort bodies are significantly bluer than the TNO populations. Comet BB shares this deviation from the TNO colors, in fact appearing a bit more neutral than the few other well-measured Oort cloud migrants.

If the flux measurements in these ≤ 2018 exposures were significantly contaminated with comae rather than being predominantly nuclear, we might expect the measured H to increase as the comet approaches the Sun. In Figure 4, we present the H_r averaged over all photometric observations from a given season. Exposures from band b are shifted to the r band using the $H_r - H_b$ from the posterior maximization above. An rms error of $0.20/\sqrt{2}$ mag is added in quadrature to each measurement error to include noise from random sampling of a sinusoidal light curve. While the year-to-year means of the DES observations are formally inconsistent with a constant magnitude, the potential year-scale variation is small (≈ 0.1 mag) and shows no long-term trend. Indeed, the 2010 VISTA observation is consistent with a constant magnitude as well, so there is no evidence for a brightening of BB’s absolute magnitude as it moves from $r_h = 34.1$ to 23.7 au for apertures of $\approx 1''$ size.

Under the assumption that the $H_r = 7.96$ derived above is entirely from a spherical nucleus with geometric albedo in the r band of p_r and density ρ , the diameter, mass, and escape velocity of BB are

$$D = \left(\frac{p_r}{0.04} \right)^{-1/2} 155 \text{ km}, \quad (9)$$

$$m = \left(\frac{p_r}{0.04} \right)^{-3/2} \left(\frac{\rho}{1 \text{ g cm}^{-3}} \right) 2.0 \times 10^{18} \text{ kg}, \quad (10)$$

and

$$v_{\text{esc}} = \left(\frac{p_r}{0.04} \right)^{-1/2} \left(\frac{\rho}{1 \text{ g cm}^{-3}} \right)^{1/2} 58 \text{ m s}^{-1}. \quad (11)$$

At the nominal assumed albedo, this makes BB a factor of 2.5 larger in diameter than C/1995 O1 (Hale-Bopp) (Fernández 2002),

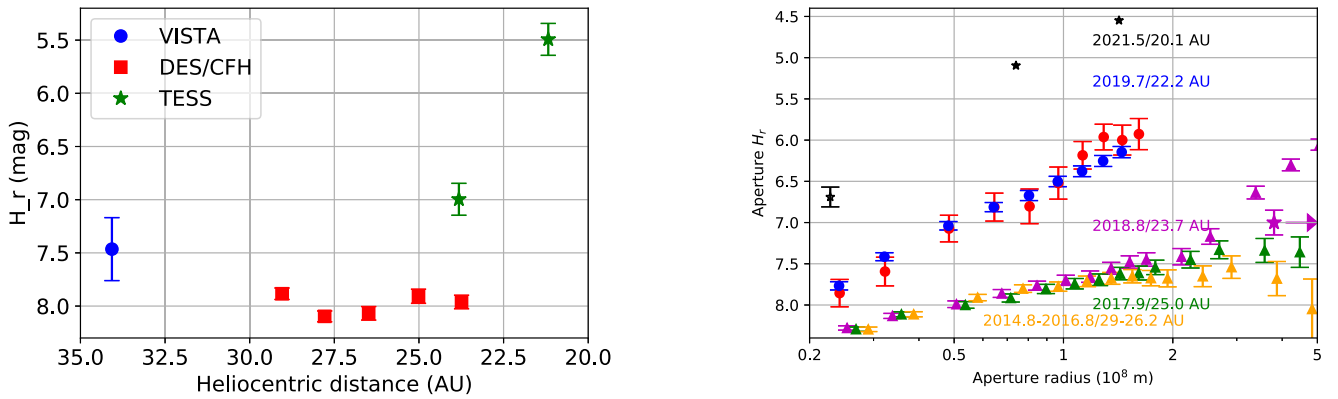


Figure 4. Left: annual average absolute point-source magnitudes from ground-based surveys, transformed to the r band using the measured colors, plotted vs. heliocentric distance as the blue circles and red squares. Bright is up, and time advances to the right. These points, which exclude any resolved coma and, we argue, are accurate nuclear magnitudes, are consistent with no overall brightening during the approach from 34 to 22 au. The TESS data (green stars), however, show a highly significant brightening of 1.5 mag between 23 and 21 au (2018–2020). Furthermore, the earlier TESS epoch shows significantly higher flux than the contemporaneous DES measurements, suggesting the presence of a growing, diffuse coma detected within the much larger photometric aperture of TESS. Right: curves of growth of BB’s absolute magnitude vs. physical aperture radius, with the epoch and r_h as labeled. From the bottom up, the triangles are from DES data, divided into three time periods as labeled. The magenta star is the TESS observation during the final DES season, which has an aperture radius of $\approx 10^9$ m. The blue and red circles are from PS1 observations in the w and i bands, respectively, on two different nights of 2019 August. The black stars are aperture data taken in 2021 June by Kokotanekova et al. (2021a; with error bar) and Dekelver (2021; no uncertainties specified). In all cases, the curve of growth of the stellar sources is flat at radii $\gtrsim 7 \times 10^7$ m. The presence of activity is detectable at large radii in images as early as 2017. The rise of the 2018 curve beyond 3×10^8 m could be an artifact of sky subtraction, but the curve is consistent with the ≈ 1 mag difference between contemporaneous TESS and DES in the left panel.

another LPC that is the largest of any comet in the past century (Lamy et al. 2004) and had $H_r \approx 9.7$ at incoming $r_h = 6.4$ au (Szabó et al. 2012). Interestingly, this places BB at a comparable size to the 160–180 km diameter estimated for the active Centaur (2060) Chiron using occultation data (Bus et al. 1996; Sickafoose et al. 2020). It will be of interest to compare the behavior of these two objects of comparable size but very different dynamical pathways to active states at r_h of 10–20 au.

Of course, BB could be smaller than this if its albedo is above the canonical $p_r = 0.04$, e.g., if it has extensive clean ice patches on its surface.

4. Coma Development

The TESS photometry, plotted as stars in the left panel of Figure 4, shows a definitive 1.5 mag increase in H during the 2 yr journey from $r_h = 23.8$ to 21.2 au, after the DES observations end, from which we infer an increase in activity before the 2021 June discovery of the coma at $r_h = 20.2$ au. More surprisingly, the TESS images from 2018 show a substantially brighter H than the DES photometry at the same time period, by $\approx 1.0 \pm 0.15$ mag. Furthermore, Farnham (2021) reported that the 2018 TESS images are resolved, with a Gaussian fit yielding $\text{FWHM} \approx 2.92$ of the $21''$ pixels, while unresolved sources are ≤ 2.06 pixels. A simple quadrature subtraction suggests that the intrinsic comet angular size is at least 2.06 pixels = $43''$, e.g., a Gaussian with $\sigma > 18''$. A coma of this size would have gone undetected in the DES scene-modeling photometry if the coma did not have a strong central concentration in the inner $1''$ – $2''$.

With this in mind, we reanalyze the DES and PS1 images from 2019 for signs of $10''$ -scale emission and demonstrate that the coma responsible for the TESS excess over DES point-source flux estimates is in fact highly resolved. Figure 4 (right) shows the curves of growth derived from aperture photometry of these images, as well as 2021 June observations reported by Dekelver (2021) and Kokotanekova et al. (2021a). A detectable coma was already present in the PS1 images at $r_h = 22.6$ au,

and indeed also for most of the DES observations, albeit not at a level that precludes our attribution of the PSF-fitting fluxes to the nucleus.

The curve of growth from the DES 2018 season is plausibly consistent with the measured TESS magnitude made in its $(5 \times 21)''$ square aperture during the same season. Post-DES imaging clearly shows an exponential increase in coma brightness, which we will quantify below.

We take a closer look at the structure and history of the coma during the DES epochs using the residual images produced by the scene-modeling photometry after subtraction of the static sky background and the best-fit central point source. Each image is scaled to the r band assuming solar colors; unfortunately, we have insufficient S/N to meaningfully constrain the coma color. Residual artifacts from defects, cosmic rays, and misregistration are masked. Figure 5 shows the inverse-variance-weighted average of these, split between the first three seasons ($r_h > 26$ au) and the last two ($r_h < 26$ au). Growth of a tail or asymmetric coma during this epoch is visible. An antisolar tail would point downward in this image stack; the observed diffuse light is $\approx 40^\circ$ away from antisolar.

More quantitative measures of the growth of the coma are plotted in Figure 6. The left panel shows the results in the observational space of surface brightness in annular bins of radius. The surface brightness I scaling with radius $I \propto \rho^{-n}$ is consistent with either a “stationary” coma, $n = 1$, as expected if dust particles move ballistically at fixed v_d from the nucleus, or $n = 1.5$, as is suggested by models of radiation pressure-dominated escape (Jewitt & Meech 1987). We are pleased to see that the coma is well measured even at a surface brightness below $30 \text{ mag arcsec}^{-2}$, which generates $< 0.004 e \text{ s}^{-1} \text{ pixel}^{-1}$ in the images, a tribute to the quality of the image calibration and background subtraction in the scene-modeling method.

Before delving into further characterization of the coma, we summarize the arguments for the DES point-source magnitudes to be dominated by nuclear flux. These return magnitudes in the r band in the range 20.7–21.6 within an effective aperture of radius $1''$ or less. The surface brightness of the coma would

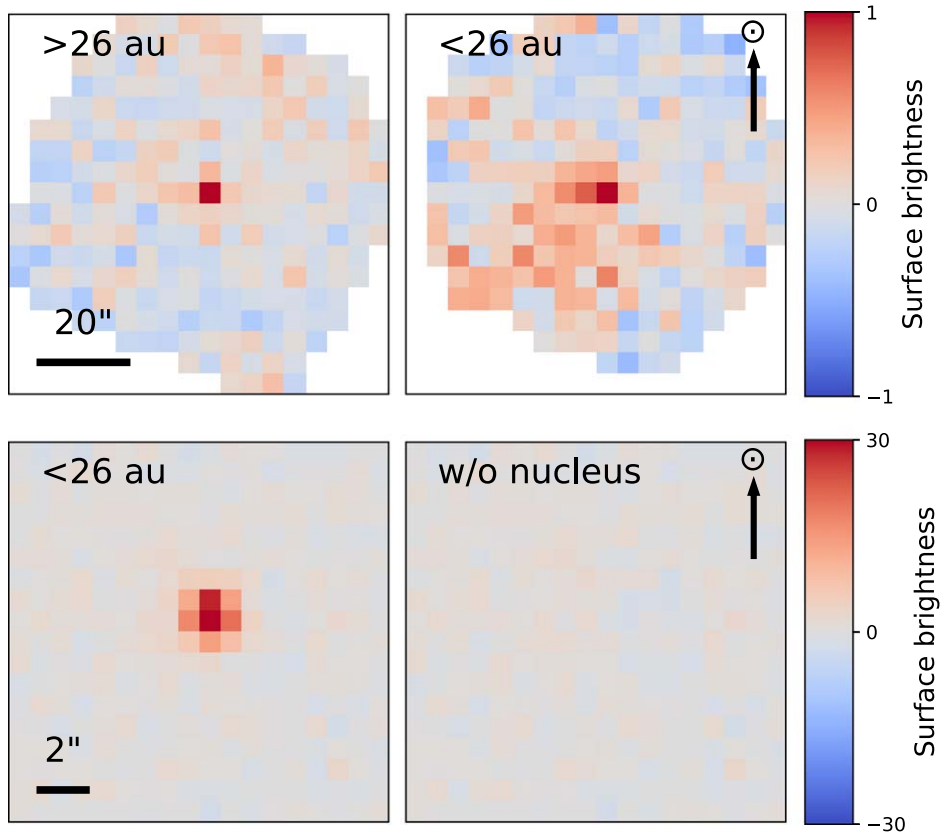


Figure 5. Top row: DES images of BB taken exterior (left) and interior (right) to $r_h = 26$ au displayed on the same angular and flux scales. These are residual images after subtraction of the background model from each exposure. All images are scaled to the r band using solar colors, inverse variance-weighted, rotated such that the projected direction toward the Sun is vertical, and binned to an $\approx 4''.5$ pixel size. The development of a tail or coma during the DES observations is apparent, but it is not precisely aligned with the antisolar vector. Bottom row: zoomed images into the central pixel of the top right image, shown at a $30\times$ coarser surface brightness scale, before (left) and after (right) the subtraction of a central point-source model. The coma is very dim compared to the point source, which we thus presume is dominated by nuclear flux.

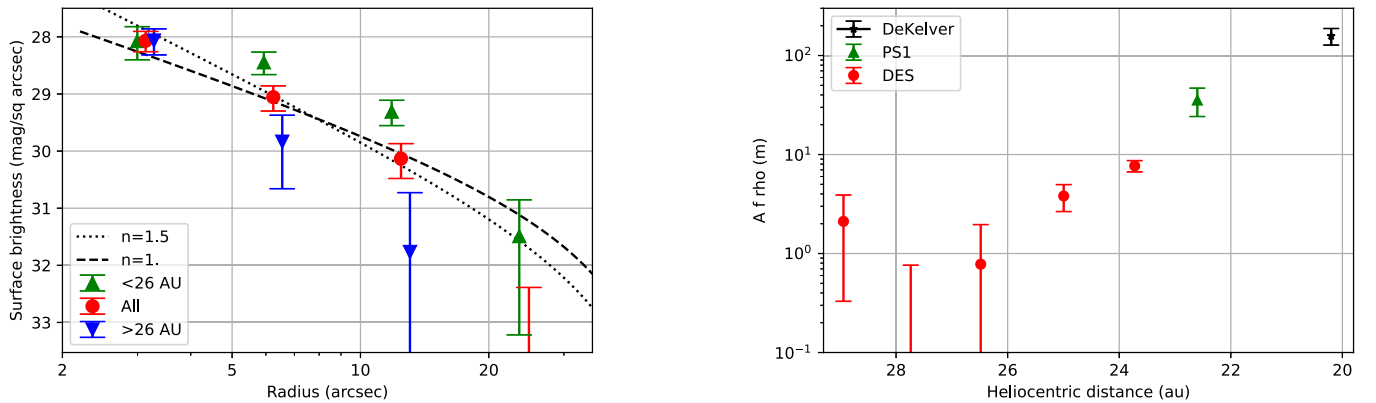


Figure 6. Left: surface brightness of the coma in annular bins as measured from DES images. (Some measures at the outermost bin are negative.) The average over all DES exposures is shown, as well as split into data before 2017 ($29 \text{ au} > r_h > 26 \text{ au}$) and in 2017–2018 ($26 \text{ au} > r_h > 23 \text{ au}$). The curves show models with surface brightness $I \propto \rho^{-n}$ for $n = 1$, as expected for a stationary coma, and $n = 1.5$, as expected for a radiation pressure-driven dust coma. Either is consistent with the data. In the right panel, under the stationary coma model, the inferred $Af\rho$ is plotted against r_h for each DES observing season and for later observations with well-defined aperture magnitudes. The coma reflectivity grows exponentially with decreasing r_h .

need to be $\approx 24 \text{ mag arcsec}^{-2}$ at a radius of $\approx 1''$ to contribute even 10% of the measured point-source flux. This would require a 4 mag drop in surface brightness between $1''$ and $2''.5$ radii, according to the left panel of Figure 6. This would be unusual behavior. It could occur transiently because of a dust outburst, but, as noted above, the dust dispersal time is months, while the photometry is stable to 20% over years. Something

exotic, such as gravitationally bound dust particles, would seem to be required to contaminate the point-source fluxes with nonnuclear light, even though both TESS and DES data indicate the presence of a detectable coma during the later years of DES.

The standard measure of coma surface brightness is $Af\rho$, where A is the geometric albedo and f is the filling factor of the

reflecting particles, conventionally measured as the average $f(<\rho)$ interior to radius ρ . For a stationary coma, this quantity is invariant with the distances from the source, the Sun, and the observer (A’Hearn et al. 1984; Fink & Rubin 2012). We transform the surface brightness into $Af\rho$ via

$$I(\rho) = \frac{Af(<\rho)}{2} \frac{L_\odot}{16\pi^2 r_h^2} \quad (12)$$

$$\Rightarrow Af\rho = 2 \times 10^{0.4(M_\odot - m_{\text{SB}})} 4\pi\rho \left(\frac{r_h}{10 \text{ au}}\right)^2, \quad (13)$$

where M_\odot is the absolute magnitude of the Sun, and m_{SB} is the observed surface brightness per arcsec². The right panel of Figure 6 plots the $Af\rho$ inferred from fitting a stationary coma model to each DES exposure at radii $\geq 4''$ from the nucleus and averaging over each season’s observations. This is plotted versus r_h , and we include values taken from later observations. From Dekelver (2021), we take the uncertainty to be the span of $Af\rho$ values determined at different radii. For the PS1 observations, we apply a generous $\pm 30\%$ standard error. The data exhibit an exponential increase in the dust content of the coma, growing $\approx 2\times$ with each au reduction in r_h . The TESS data even exhibit this rate of brightening within the duration of its 2020 observing (8% per month). At $r_h > 26$ au, the uncertainties are large enough to admit a wide variety of behavior, e.g., even a constant coma surface brightness as might occur if BB entered the inner solar system with a gravitationally bound “dirtmosphere” of particles accumulated through impacts over millions of years.

5. Discussion

Comet BB has uniquely high-quality photometric data through the initial growth period of its coma, with direct detections of the coma out to $r_h \approx 26$ au. We expect future work to produce detailed thermal and dynamical modeling of the comet, but here we show that a very simple sublimation model fits the observations well. We have not investigated activity powered by phase changes or annealing of ices, such as crystallization of amorphous water ice (e.g., Prialnik et al. 2004).

5.1. Sublimating Species

For a single species with molecular mass m_{mol} sublimating into vacuum from a surface, the mass-loss rate per unit area A is

$$\dot{m} \equiv \frac{\dot{M}}{A} = P_{\text{sat}} \sqrt{\frac{m_{\text{mol}}}{2\pi kT}} \quad (14)$$

$$\propto e^{-\Delta H/RT} \sqrt{\frac{m_{\text{mol}}}{2\pi kT}} \quad (15)$$

$$\Rightarrow \log \dot{M} \sqrt{T} = \text{const} - \frac{\Delta H}{RT}, \quad (16)$$

where P_{sat} is the saturation vapor pressure, and we use the Clausius–Clapeyron formula to express its dependence on temperature T in Equation (15). Here ΔH is the enthalpy of sublimation (which we assume varies little with T), and R is the ideal gas constant.

Under radiative equilibrium with negligible heat conduction with the cometary interior and negligible heat loss to

sublimation, a section of the surface attains a temperature T with

$$\epsilon\sigma T^4 = \frac{L_\odot}{4\pi r_h^2} (1-p) \langle \cos\theta \rangle \quad (17)$$

$$\Rightarrow T = \left[\frac{(1-p)\langle \cos\theta \rangle}{\epsilon} \right]^{1/4} \left(\frac{L_\odot}{4\pi\sigma(1 \text{ au})^2} \right)^{1/4} \left(\frac{r_h}{1 \text{ au}} \right)^{-1/2} \quad (18)$$

$$= \eta \times (397 \text{ K}) \left(\frac{r_h}{1 \text{ au}} \right)^{-1/2}. \quad (19)$$

In these equations, σ is the Stefan–Boltzmann constant, p is the Bond albedo of the surface (nominally 0.04), and ϵ is the infrared emissivity (nominally 0.9). With θ as the angle between illumination and the normal, the average $\langle \cos\theta \rangle$ over the thermal timescale for the warmest part of the comet (which will dominate the sublimation rate at low T) will be between 1 (at the subsolar point for a short thermal time constant or a pole-on rotator) and $1/\pi$ for the equator of an orthogonal rotator with a long time constant. We bundle all of these physical/geometric constants in the first term of Equation (18) into a factor η , which is nominally close to unity but could be as low as ≈ 0.75 .⁵⁵

The third part of the simple model is to relate the coma brightness $Af\rho$ to the sublimation rate. If the scattering is dominated by solid particles with albedo p_d , radius a_d , near-spherical geometric cross section, density ρ_d , production rate \dot{M}_d , and velocity v_d , then

$$Af\rho = \frac{3p_d \dot{M}_d}{8\pi a_d \rho_d v_d}. \quad (20)$$

If we assume that p_d , a_d , ρ_d , and the dust-to-gas ratio $\chi = \dot{M}_d/\dot{M}$ are independent of heliocentric distance over the 20–30 au range, we obtain a scaling

$$Af\rho \propto \dot{M}/v_d. \quad (21)$$

Note that this proportionality does not require the geometric scattering limit to hold, only that the scattering per unit mass of dust is time-invariant, i.e., no grain destruction or breakdown. Combining this with Equation (16) yields

$$\log(Af\rho v_d T^{1/2}) = \text{const} - \frac{\Delta H}{RT}. \quad (22)$$

One working assumption for v_d is that it will scale with the thermal velocity, i.e., $\propto T^{1/2}$. A stronger dependence would be expected if the dust velocity is driven by radiation pressure: $v_d \propto r_h^{-2} \propto T^4$.

The left panel of Figure 7 plots $Af\rho v_d T^{1/2}$ on the (logarithmic) y -axis versus $1/T$ on the x -axis, assuming radiative equilibrium for T and $v_d \propto v_{\text{th}}$. Per Equation (22), the data should follow a line with slope $-\Delta H/R$ on this plot for sublimation of a single species. The data are seen to be consistent with this model, with a value of ΔH that depends on whether we take the fast- or slow-rotator limit for η in the radiative equilibrium formula.

⁵⁵ This η is not the same quantity as the beaming parameter η that appears in more sophisticated asteroid thermal models (Lebofsky et al. 1986; Harris 1998).

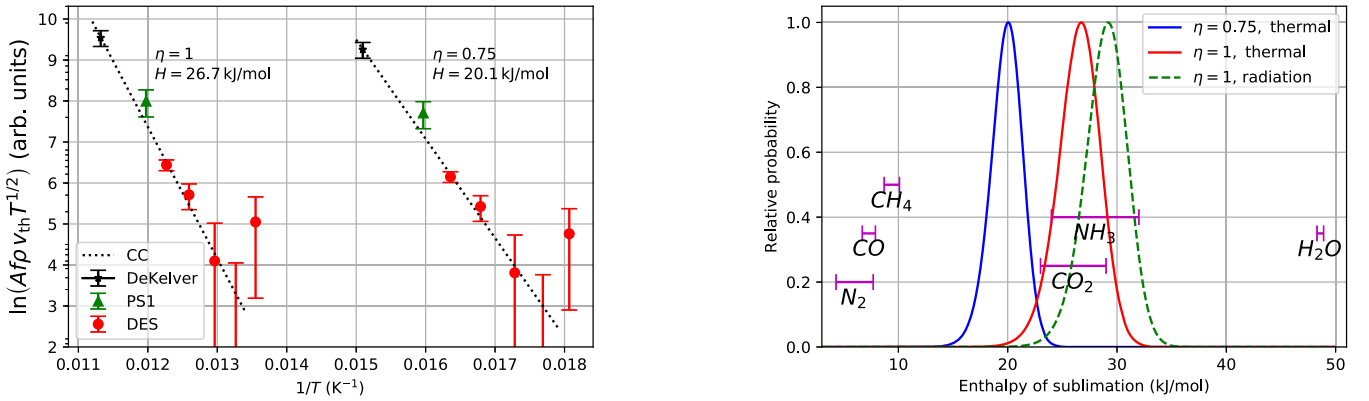


Figure 7. In the left panel, following Equation (22) and assuming radiative equilibrium temperatures, we plot the log of $Af\rho v_{\text{th}}\sqrt{T}$ vs. $1/T$, which should yield a straight line if the coma’s scattering strength is proportional to the sublimation rate of a single species following the Clausius–Clapeyron (CC) relation. For either the fast- or slow-rotator bounds on radiative equilibrium ($\eta = 0.75, 1$), the data are well fit by such a form. Right: relative probability of the enthalpy of sublimation ΔH in a fit of Equation (22) to the measured values of $Af\rho$, marginalizing over the scaling constant. The solid red curve gives the nominal case, with $\eta = 1$ and a dust velocity scaling with the thermal velocity. The solid blue curve assumes a fast-rotating limit ($\eta = 0.75$), and the dashed green curve assumes dust velocities scaling with radiation pressure ($v_d \propto T^4$). The enthalpies of sublimation of the potential cometary volatiles are marked; the data strongly favor CO_2 or NH_3 as the driver of BB’s mass loss to date.

The right panel of Figure 7 plots the result of a quantitative fit of Equation (22) to the $Af\rho$ measurements as a function of ΔH , marginalizing over the unknown constant. In the nominal (red) case, the inferred enthalpy of sublimation is fully consistent with the lab-measured values for NH_3 and/or CO_2 and clearly inconsistent with the more volatile species N_2 , CH_4 , and CO . As is well known, H_2O is ruled out as a volatile at these distances as well. The values of ΔH are taken from Luna et al. (2014) and Feistel & Wagner (2007). The dashed green curve changes the scaling of v_d versus T from thermal to radiation-pressure laws and does not change the conclusion. Moving to the fast-rotator value $\eta = 0.75$ yields proportionately lower ΔH values, still better associated with CO_2 and NH_3 .

The coma growth rate is thus strongly suggestive of activity powered by CO_2 and/or NH_3 sublimation at $20 \text{ au} < r_h < 25 \text{ au}$, with slow and/or pole-on rotation somewhat favored to yield higher peak surface temperatures. Across the range of potential surface temperatures, the mass-loss rate per square meter from pure CO_2 is $>100\times$ larger than that from a pure NH_3 ice surface, so CO_2 would have to be far less abundant than NH_3 in order for the latter to be driving the activity rate in pure-ice forms.

At $r_h > 25 \text{ au}$, the coma is too weak to be well measured in the data. It is possible that more volatile species (N_2 , CH_4 , or CO) could have dominated sublimation at these times. These latter species, however, have orders-of-magnitude higher vapor pressure (and specific sublimation rates) than CO_2 and NH_3 at $T = 78 \text{ K}$, the $\eta = 1$ subsolar temperature for $r_h = 25 \text{ au}$. Any surface abundance in their pure-ice forms on the surface of BB must be very low relative to the CO_2/NH_3 that appears to dominate sublimation at $r_h \leq 25 \text{ au}$. A scenario that economically ties the dynamical and thermodynamic results above is that these more volatile species were heavily sublimated from BB during its previous perihelion passage to $\approx 18 \text{ au}$, leaving behind a crust that is largely depleted in these most volatile species. Or perhaps this depletion is a remnant of the thermal environment at the original location of formation of BB.

5.2. Dust Production

The dynamics of dust production on BB are made more interesting by the fact that the escape velocity of $\approx 60 \text{ m s}^{-1}$ is

above or comparable to the dust velocities estimated for other comets, e.g., $< 50 \text{ m s}^{-1}$ for Comet Boattini (Hui et al. 2019) or $\approx 4 \text{ m s}^{-1}$ for C/2017 K2 (Jewitt et al. 2019). The low sublimation rates and pressures for BB at $r_h > 22 \text{ au}$ may limit the size of particles that can be raised and attain escape by the gas, and/or the coma may be dominated by small grains that are driven to escape by radiation pressure. The coma is observed to be asymmetric in its 2021 observations, the 2018 DES data (Figure 5), and potentially the TESS observations (Farnham 2021), implicating radiation pressure or tidal escape mechanisms for the dust. High-quality imaging of the coma as soon as possible would be of great interest in constraining the dust size and dynamics.

If a fraction f_{active} of the surface of BB is sublimating CO_2 at the rates described in Equation (14), then the gas mass-loss rate from BB rises from $400f_{\text{active}}$ to $7 \times 10^4 f_{\text{active}} \text{ kg s}^{-1}$ when closing from 26 to 20 au. This assumes $\eta \approx 1$ (slow rotator) and the vapor pressure cited by Fray & Schmitt (2009). A nonporous, pure- CO_2 ice patch at the subsolar point would be eroded by 0.1 mm yr^{-1} at 26 au, increasing to 2 cm yr^{-1} at its current $r_h \approx 20 \text{ au}$.

Adopting the simplistic model of Equation (20) and a uniform streaming velocity $v_d = f_v v_{\text{th}}$, where v_{th} is the rms 1D thermal velocity of a CO_2 molecule, we can solve for the dust particle radius as

$$a_d = \sqrt{\frac{9}{8\pi} \frac{p_d \chi f_{\text{active}} P_{\text{sat}} a_{\text{BB}}^2 m_{\text{mol}}}{f_v \rho_d [Af\rho] kT}} \quad (23)$$

$$\approx \left(\frac{p\chi}{0.04}\right) \left(\frac{0.1}{f_v}\right) \left(\frac{f_{\text{active}}}{0.1}\right) \times 10 \mu\text{m}. \quad (24)$$

We take a_{BB} as the nominal radius of the comet, m_{mol} as the mass of a CO_2 molecule, albedos of $p = 0.04$ for both the comet and its debris, and the observed values of $Af\rho$ to obtain Equation (24). The nominal values of χ , f_{active} , and f_v are ill-supported order-of-magnitude estimates. The implied dust particle radius may even be overestimated, as the assumption of $f_{\text{active}} = 0.1$ of the surface being CO_2 ice near the subsolar temperature may be an overestimate. It nonetheless suggests that the coma has small particles, indeed small enough that the

assumption of a geometric scattering cross section needs to be relaxed. Small dust particles might be expected because of the anemic gas flow density and the importance of radiation pressure in overcoming BB’s gravity. Clearly, a more detailed model of the dust dynamics would be of interest.

5.3. Comparison to Other Distant LPCs

Opportunities to study incoming comets at $r_h > 20$ au have been rare enough that there is no definition of “typical” behavior. It is already clear that the behavior is diverse. It is good to keep in mind that selection biases will favor the discovery at large distances of comets that are unusually active or, like BB, unusually large.

Comet C/2017 K2 (PanSTARRS), hereafter K2, has a similar aphelion and inclination to BB, but Królikowska & Dybczyński (2018) reported it to have a 97% chance of having passed within $r_h < 10$ au on its previous passage. It was discovered at $r_h = 16$ au, but pre-discovery images at $r_h = 24$ au also display a coma (Hui et al. 2018).

Comet K2 is much smaller than BB, with an estimated nuclear radius of < 9 km (Jewitt et al. 2017). These authors inferred K2’s coma to be comprised of millimeter-scale particles moving at speeds of $\approx 4 \text{ m s}^{-1}$ —which would probably not escape BB—and estimate that K2 has been expelling such particles at a relatively steady and isotropic rate since $r_h \approx 30$ au. This is in stark contrast to BB’s exponentially growing scattering cross section in the 20–30 au range.

Comet C/2010 U3 (Boattini) was discovered inbound at $r_H = 18.4$ au and found on earlier images at $r_h = 25.8$ and 24.6 au with a visible coma (Hui et al. 2019). Like K2, Boattini is thought to have had its previous perihelion at < 10 au, yet its coma behavior is quite distinct from K2’s, showing intermittent outbursts and a tail inferred to be composed of much smaller particles than K2’s.

Comets K2, Boattini, and BB display very diverse activity patterns at $r_h > 15$ au. Comet K2 has a steady, large-particle coma, Boattini exhibits outbursts and a tail, and BB undergoes exponential growth in cross section over this period that is consistent with simple sublimation thermodynamics of carbon dioxide and/or ammonia. There is also diversity in the apparent role of CO in distant activity. CO emission has been detected from K2 at 7 au (incoming; Yang et al. 2021), and CO was detected in the coma of the large LPC Hale-Bopp and inferred to drive its activity at distances as large as 26 au (Gunnarsson et al. 2003; Szabó et al. 2008). Womack et al. (2017) reviewed the data on CO emission at distances of 4–11 au for Hale-Bopp, Chiron, and 29P/Schwassmann-Wachmann 1 (another active Centaur) and concluded that CO drives activity in all three objects, albeit with very diverse temporal behavior. This makes the current agreement of BB’s coma growth with CO₂ ice sublimation, rather than pure CO ice sublimation, of interest; is there a skin-deep lack of CO, such that large quantities of buried CO could be liberated as fresh material is uncovered nearer perihelion? Searches for CO sublimation in the coming years are clearly desirable.

No generalized pattern is apparent yet for the behavior of distant LPCs, aside from the existence of activity in some form out to ≈ 30 au. Even this ubiquity can be explained by selection effects on a more diverse population.

6. Summary

Comet BB is arguably the largest comet ever discovered and the first with useful observations obtained before it has ever come closer than 18 au to the Sun. Assuming a typical albedo, its diameter of ≈ 150 km implies a mass $10\times$ larger than Hale-Bopp and capable of gravitationally binding many of the larger particles ejected from other comets. The object is at present 20 au from the Sun, and its previous perihelion was likely at $\gtrsim 18$ au, so this may be the only comet ever measured before any approach to $r_h < 10$ au. Its nucleus has nearly gray reflectivity, in common with (or slightly bluer than) previously observed objects with Oort cloud origins.

Variation in the absolute magnitude of the nucleus is strongly detected and consistent with a ± 0.20 mag sinusoidal light curve. The data are too sparse to actually derive a light curve, and it is certainly possible that some of this variability is due to unresolved small dust outbursts, so that the true nuclear variation is even smaller than $\pm 20\%$.

We are able to detect the presence of activity in DES images starting with the 2017 season, at $r_h \approx 25$ au, which grows exponentially while approaching $r_h = 20$ au. The rate of growth is consistent with sublimation of a species with an enthalpy of sublimation near the 26 kJ mol^{-1} of CO₂ (or NH₃). The coma measurements at $r_h > 25$ au have too low an S/N to characterize the behavior, so these earlier phases of activity could, e.g., be dominated by other species’ sublimation. Comet BB is thus an outlier among the (notoriously unpredictable) population of comets in that its onset of activity follows simple sublimation thermodynamics to date; i.e., it is (so far) a “spherical cow.” Perhaps this behavior is related to the fact that it is also an outlier in size and in its relatively uneventful past thermal history.

It is usually a losing proposition to speculate on the future behavior of comets, even one such as BB, whose activity has followed a simple model to date. Indeed, while this paper was under review, monitoring of BB in mid-2021 showed nonmonotonic brightness with obvious outbursts (Kelley et al. 2021; Kokotanekova et al. 2021b). Nonetheless, the overall pattern of exponential growth in the coma over the preceding years remains valid. We heedlessly proceed to estimate BB’s brightening if its scattering cross section continues to grow in proportion to the CO₂ sublimation rate in radiative equilibrium as it reaches its 11 au perihelion in a decade. The CO₂ sublimation rate will grow to a level at which most of the incident solar flux is turned to sublimation enthalpy. The mass-loss rate then scales with the fraction of the surface material composed of CO₂ ice near the subsolar point. If this is 10%, then the sublimation rate will be $\gtrsim 200\times$ above its value in 2021 June. Combined with the r_h^{-4} brightening, BB would be 8.5 mag brighter in apparent magnitude at perihelion than the magnitude $G \approx 17.5$ currently reported in large apertures (Dekelver 2021), i.e., $G \approx 9$, a bit fainter than Titan. If a water-ice crust forms and blocks CO₂ sublimation, the coma will be suppressed. If the CO₂ sublimation spreads across more of the comet’s surface, it can be substantially brighter. It will be an impressive telescopic target, and its large surface area may generate a substantial CO₂-powered coma and tail despite remaining far outside the water-ice line.

The catalog of distant incoming Oort cloud comets is likely to grow rapidly in the next decade, as the Vera C. Rubin Observatory Legacy Survey of Space and Time will easily detect and track any object of half BB’s size that comes within

$r_h \lesssim 40$ au in the next decade, even those with no activity, obtaining hundreds of exposures in multiple bands for each.

We thank Gonzalo Tancredi and Jim Annis for careful reviews of this work before submission, and we also thank the anonymous referee and the editor, Maria Womack, for useful suggestions during the journal submission. University of Pennsylvania authors have been supported in this work by grants AST-1515804 and AST-2009210 from the National Science Foundation and grant DE-SC0007901 from the Department of Energy.

Pan-STARRS is supported by the National Aeronautics and Space Administration under grant No. 80NSSC18K0971 issued through the SSO Near Earth Object Observations Program.

This research has made use of the services of the ESO Science Archive Facility. Based on observations collected at the European Southern Observatory under ESO program 179. A-2004(C). This work also makes use of public data from the Canada–France–Hawaii Telescope Science Archive.

This paper includes data collected by the TESS mission, which are publicly available from the Mikulski Archive for Space Telescopes (MAST). Funding for the TESS mission is provided by NASA’s Science Mission directorate.

Funding for the DES Projects has been provided by the U.S. Department of Energy, the U.S. National Science Foundation, the Ministry of Science and Education of Spain, the Science and Technology Facilities Council of the United Kingdom, the Higher Education Funding Council for England, the National Center for Supercomputing Applications at the University of Illinois at Urbana-Champaign, the Kavli Institute of Cosmological Physics at the University of Chicago, the Center for Cosmology and Astro-Particle Physics at the Ohio State University, the Mitchell Institute for Fundamental Physics and Astronomy at Texas A&M University, Financiadora de Estudos e Projetos, Fundação Carlos Chagas Filho de Amparo à Pesquisa do Estado do Rio de Janeiro, Conselho Nacional de Desenvolvimento Científico e Tecnológico and the Ministério da Ciência, Tecnologia e Inovação, the Deutsche Forschungsgemeinschaft, and the Collaborating Institutions in the Dark Energy Survey.

The Collaborating Institutions are Argonne National Laboratory, the University of California at Santa Cruz, the University of Cambridge, Centro de Investigaciones Energéticas, Medioambientales y Tecnológicas-Madrid, the University of Chicago, University College London, the DES-Brazil Consortium, the University of Edinburgh, the Eidgenössische Technische Hochschule (ETH) Zürich, Fermi National Accelerator Laboratory, the University of Illinois at Urbana-Champaign, the Institut de Ciències de l’Espai (IEEC/CSIC), the Institut de Física d’Altes Energies, Lawrence Berkeley National Laboratory, the Ludwig-Maximilians Universität München and the associated Excellence Cluster Universe, the University of Michigan, NSF’s NOIRLab, the University of Nottingham, The Ohio State University, the University of Pennsylvania, the University of Portsmouth, SLAC National Accelerator Laboratory, Stanford University, the University of Sussex, Texas A&M University, and the OzDES Membership Consortium.

Based in part on observations at Cerro Tololo Inter-American Observatory at NSF’s NOIRLab (NOIRLab Prop. ID 2012B-0001; PI: J. Frieman), which is managed by the

Association of Universities for Research in Astronomy (AURA) under a cooperative agreement with the National Science Foundation.

The DES data management system is supported by the National Science Foundation under grant Nos. AST-1138766 and AST-1536171. The DES participants from Spanish institutions are partially supported by MICINN under grants ESP2017-89838, PGC2018-094773, PGC2018-102021, SEV-2016-0588, SEV-2016-0597, and MDM-2015-0509, some of which include ERDF funds from the European Union. IFAE is partially funded by the CERCA program of the Generalitat de Catalunya. Research leading to these results has received funding from the European Research Council under the European Union’s Seventh Framework Program (FP7/2007–2013), including ERC grant agreements 240672, 291329, and 306478. We acknowledge support from the Brazilian Instituto Nacional de Ciência e Tecnologia (INCT) do e-Universo (CNPq grant 465376/2014-2).

This manuscript has been authored by the Fermi Research Alliance, LLC, under contract No. DE-AC02-07CH11359 with the U.S. Department of Energy, Office of Science, Office of High Energy Physics. The United States Government retains and the publisher, by accepting the article for publication, acknowledges that the United States Government retains a non-exclusive, paid-up, irrevocable, worldwide license to publish or reproduce the published form of this manuscript, or allow others to do so, for United States Government purposes.


Facilities: Blanco, TESS, PS1, CFHT.

Software: WHFast (Wisdom & Holman 1991; Rein & Tamayo 2015), REBOUND (Rein & Liu 2012), REBOUNDx (Tamayo et al. 2020), Astropy (Astropy Collaboration 2013, 2018), Matplotlib (Hunter 2007).

ORCID iDs

Pedro H. Bernardinelli  <https://orcid.org/0000-0003-0743-9422>

Gary M. Bernstein  <https://orcid.org/0000-0002-8613-8259>

Benjamin T. Montet  <https://orcid.org/0000-0001-7516-8308>

Robert Weryk  <https://orcid.org/0000-0002-0439-9341>

Richard Wainscoat  <https://orcid.org/0000-0002-1341-0952>

M. Aguena  <https://orcid.org/0000-0001-5679-6747>

J. Annis  <https://orcid.org/0000-0002-0609-3987>

E. Bertin  <https://orcid.org/0000-0002-3602-3664>

D. Brooks  <https://orcid.org/0000-0002-8458-5047>


J. Carretero  <https://orcid.org/0000-0002-3130-0204>

R. Cawthon  <https://orcid.org/0000-0003-2965-6786>


C. Conselice  <https://orcid.org/0000-0003-1949-7638>

M. Costanzi  <https://orcid.org/0000-0001-8158-1449>


H. T. Diehl  <https://orcid.org/0000-0002-8357-7467>


J. Garcia-Bellido  <https://orcid.org/0000-0002-9370-8360>

E. Gaztanaga  <https://orcid.org/0000-0001-9632-0815>

D. W. Gerdes  <https://orcid.org/0000-0001-6942-2736>


R. A. Gruendl  <https://orcid.org/0000-0002-4588-6517>

J. Gschwend  <https://orcid.org/0000-0003-3023-8362>

S. R. Hinton  <https://orcid.org/0000-0003-2071-9349>

D. L. Hollowood  <https://orcid.org/0000-0002-9369-4157>

K. Kuehn  <https://orcid.org/0000-0003-0120-0808>

J. L. Marshall  <https://orcid.org/0000-0003-0710-9474>

F. Menanteau  <https://orcid.org/0000-0002-1372-2534>

R. Miquel  <https://orcid.org/0000-0002-6610-4836>

R. Morgan  <https://orcid.org/0000-0002-7016-5471>

F. Paz-Chinchón  <https://orcid.org/0000-0003-1339-2683>
 A. Pieres  <https://orcid.org/0000-0001-9186-6042>
 A. Roodman  <https://orcid.org/0000-0001-5326-3486>
 I. Sevilla-Noarbe  <https://orcid.org/0000-0002-1831-1953>
 M. E. C. Swanson  <https://orcid.org/0000-0002-1488-8552>
 G. Tarle  <https://orcid.org/0000-0003-1704-0781>
 C. To  <https://orcid.org/0000-0001-7836-2261>

References

- A'Hearn, M. F., Schleicher, D. G., Millis, R. L., Feldman, P. D., & Thompson, D. T. 1984, *AJ*, **89**, 579
- Astropy Collaboration, Robitaille, T. P., & Tollerud, E. J. 2013, *A&A*, **558**, A33
- Astropy Collaboration, Price-Whelan, A. M., & Sipőcz, B. M. 2018, *AJ*, **156**, 123
- Bailer-Jones, C. A. L., Rybizki, J., Andrae, R., & Fouesneau, M. 2018, *A&A*, **616**, A37
- Bernardinelli, P., & Bernstein, G. 2021, MPEC, M53, <https://minorplanetcenter.net/mpec/K21/K21M53.html>
- Bernardinelli, P. H., Bernstein, G. M., Sako, M., et al. 2020, *ApJS*, **247**, 32
- Bernardinelli, P. H., Bernstein, G. M., Sako, M., et al. 2021, arXiv:2109.03758
- Bernstein, G., & Khushalani, B. 2000, *AJ*, **120**, 3323
- Bernstein, G. M., Armstrong, R., Plazas, A. A., et al. 2017, *PASP*, **129**, 074503
- Bertin, E., & Arnouts, S. 1996, *A&AS*, **117**, 393
- Bobylev, V. V., & Bajkova, A. T. 2020, *AstL*, **46**, 245
- Brasseur, C. E., Phillip, C., Fleming, S. W., Mullally, S. E., & White, R. L. 2019, Astrocut: Tools for Creating Cutouts of TESS Images, Astrophysics Source Code Library, ascl:1905.007
- Brout, D., Sako, M., Scolnic, D., et al. 2019, *ApJ*, **874**, 106
- Bus, S. J., Buie, M. W., Schleicher, D. G., et al. 1996, *Icar*, **123**, 478
- Buzzi, L., & Lister, T. 2021, MPEC, M83, <https://www.minorplanetcenter.net/mpec/K21/K21M83.html>
- Dekelver, P.-J. 2021, C/2014 UN271 Bernardinelli-Bernstein, http://www.astronomie.be/pieterjan.dekelver/Observations/20210629_C2014UN271_Bernardinelli-Bernstein_W86_FULL.jpg
- Demetz, L., Buzzi, L., Aletti, A., & Lister, T. 2021, Central Bureau Astronomical Telegrams, CBET-4989
- Farnham, T. 2021, ATel, **14759**, 1
- Feistel, R., & Wagner, W. 2007, *GeCoA*, **71**, 36
- Fernández, Y. R. 2002, *EM&P*, **89**, 3
- Fink, U., & Rubin, M. 2012, *Icar*, **221**, 721
- Fouchard, M. 2004, *MNRAS*, **349**, 347
- Fray, N., & Schmitt, B. 2009, *P&SS*, **57**, 2053
- Gaia Collaboration, Brown, A. G. A., Vallenari, A., et al. 2018, *A&A*, **616**, A1
- Gaia Collaboration, Brown, A. G. A., Vallenari, A., et al. 2021, *A&A*, **649**, A1
- Gunnarsson, M., Bockelée-Morvan, D., Winnberg, A., et al. 2003, *A&A*, **402**, 383
- Gwyn, S. D. J., Hill, N., & Kavelaars, J. J. 2012, *PASP*, **124**, 579
- Harris, A. W. 1998, *Icar*, **131**, 291
- Heisler, J., & Tremaine, S. 1986, *Icar*, **65**, 13
- Hui, M.-T., Farnocchia, D., & Micheli, M. 2019, *AJ*, **157**, 162
- Hui, M.-T., Jewitt, D., & Clark, D. 2018, *AJ*, **155**, 25
- Hunter, J. D. 2007, *CSE*, **9**, 90
- Jarvis, M., Bernstein, G. M., Amon, A., et al. 2021, *MNRAS*, **501**, 1282
- Jewitt, D., Agarwal, J., Hui, M.-T., et al. 2019, *AJ*, **157**, 65
- Jewitt, D., Hui, M.-T., Mutchler, M., et al. 2017, *ApJL*, **847**, L19
- Jewitt, D., Kim, Y., Mutchler, M., et al. 2021, *AJ*, **161**, 188
- Jewitt, D. C., & Meech, K. J. 1987, *ApJ*, **317**, 992
- Jewitt, D. 2015, *AJ*, **150**, 201
- Kelley, M. S. P., Lister, T., & Holt, C. E. 2021, ATel, **14917**, 1
- Kokotanekova, R., Lister, T., Bannister, M., et al. 2021a, ATel, **14733**, 1
- Kokotanekova, R., Opatom, C., Knight, M., et al. 2021b, BAAS, **53**, 301.04
- Królikowska, M., & Dybczyński, P. A. 2018, *A&A*, **615**, A170
- Lamy, P. L., Toth, I., Fernández, Y. R., & Weaver, H. A. 2004, in Comets II, ed. M. C. Festou, H. U. Keller, & H. A. Weaver (Tucson, AZ: Univ. of Arizona Press), 223
- Lebofsky, L. A., Sykes, M. V., Tedesco, E. F., et al. 1986, *Icar*, **68**, 239
- Li, C., Zhao, G., & Yang, C. 2019, *ApJ*, **872**, 205
- Luna, R., Satorre, M. Á., Santonja, C., & Domingo, M. 2014, *A&A*, **566**, A27
- Meech, K. J., Kleyana, J. T., Hainaut, O., et al. 2017, *ApJ*, **849**, L8
- Meech, K. J., Pittichová, J., Bar-Nun, A., et al. 2009, *Icar*, **201**, 719
- Oort, J. H. 1927, BAN, **3**, 275
- Prialnik, D., Benkhoff, J., & Podolak, M. 2004, in Comets II, ed. M. C. Festou, H. U. Keller, & H. A. Weaver (Tucson, AZ: Univ. of Arizona Press), 359
- Rein, H., & Liu, S. F. 2012, *A&A*, **537**, A128
- Rein, H., & Tamayo, D. 2015, *MNRAS*, **452**, 376
- Ricker, G. R., Winn, J. N., Vanderspek, R., et al. 2015, *JATIS*, **1**, 014003
- Ridden-Harper, R., Bannister, M. T., & Kokotanekova, R. 2021, *RNAAS*, **5**, 161
- Sárneczky, K., Szabó, G. M., Csák, B., et al. 2016, *AJ*, **152**, 220
- Sickafoose, A. A., Bosh, A. S., Emery, J. P., et al. 2020, *MNRAS*, **491**, 3643
- Stassun, K. G., Oelkers, R. J., Pepper, J., et al. 2018, *AJ*, **156**, 102
- Szabó, G. M., Kiss, L. L., Pál, A., et al. 2012, *ApJ*, **761**, 8
- Szabó, G. M., Kiss, L. L., & Sárneczky, K. 2008, *ApJL*, **677**, L121
- Tamayo, D., Rein, H., Shi, P., & Hernandez, D. M. 2020, *MNRAS*, **491**, 2885
- The Dark Energy Survey Collaboration, Abbott, T. M. C., & Adamów, M. 2021, *ApJS*, **255**, 20
- Vokrouhlický, D., Nesvorný, D., & Dones, L. 2019, *AJ*, **157**, 181
- Vorobiev, D., Irwin, A., Ninkov, Z., et al. 2019, *JATIS*, **5**, 041507
- Willmer, C. N. A. 2018, *ApJS*, **236**, 47
- Wisdom, J., & Holman, M. 1991, *AJ*, **102**, 1528
- Womack, M., Sarid, G., & Wierzbos, K. 2017, *PASP*, **129**, 031001
- Yang, B., Jewitt, D., Zhao, Y., et al. 2021, *ApJL*, **914**, L17